Monthly Notices of the ROYAL ASTRONOMICAL SOCIETY

MNRAS **506,** 6014–6028 (2021) https://doi.org/10.1093/mnras/stab2085
Advance Access publication 2021 July 22

An AMUSING look at the host of the periodic nuclear transient ASASSN-14ko reveals a second AGN

M. A. Tucker [1]★† B. J. Shappee [1] J. T. Hinkle [1] J. M. M. Neustadt [2] M. Eracleous [3] C. S. Kochanek [2,4] J. L. Prieto [5,6] A. V. Payne [1]‡ L. Galbany [7] J. P. Anderson [8] K. Auchettl [9,10,11] C. Auge [1] and Thomas W.-S. Holoien [12]§

[1]*Institute for Astronomy, University of Hawaii at Manoa, 2680 Woodlawn Dr., Honolulu HI 96822, USA*
[2]*Department of Astronomy, The Ohio State University, 140 West 18th Avenue, Columbus OH 43210, USA*
[3]*Department of Astronomy & Astrophysics and Institute for Gravitation and the Cosmos, The Pennsylvania State University, 525 Davey Laboratory, University Park PA 16802, USA*
[4]*Center for Cosmology and AstroParticle Physics, The Ohio State University, 191 W. Woodruff Ave., Columbus OH 43210, USA*
[5]*Núcleo de Astronomía de la Facultad de Ingeniería y Ciencias, Universidad Diego Portales, Av. Ejército 441, Santiago 8370109, Chile*
[6]*Millennium Institute of Astrophysics, Santiago, Chile*
[7]*Institute of Space Sciences (ICE, CSIC), Campus UAB, Carrer de Can Magrans, s/n, Barcelona E-08193, Spain*
[8]*European Southern Observatory, Alonso de Córdova 3107, Casilla 19, Santiago, Chile*
[9]*School of Physics, The University of Melbourne, Parkville VIC 3010, Australia*
[10]*ARC Centre of Excellence for All Sky Astrophysics in 3 Dimensions (ASTRO 3D), Sydney, Australia*
[11]*Department of Astronomy and Astrophysics, University of California, Santa Cruz CA 95064, USA*
[12]*The Observatories of the Carnegie Institution for Science, 813 Santa Barbara St., Pasadena CA 91101, USA*

Accepted 2021 July 12. Received 2021 July 5; in original form 2020 November 13

ABSTRACT

We present Multi-Unit Spectroscopic Explorer (MUSE) integral-field spectroscopy of ESO 253−G003, which hosts a known active galactic nucleus (AGN) and the periodic nuclear transient ASASSN-14ko, observed as part of the All-weather MUse Supernova Integral-field of Nearby Galaxies survey. The MUSE observations reveal that the inner region hosts two AGN separated by 1.4 ± 0.1 kpc ($\approx 1\farcs7$). The brighter nucleus has asymmetric broad permitted emission-line profiles and is associated with the archival AGN designation. The fainter nucleus does not have a broad emission-line component but exhibits other AGN characteristics, including $v_{\rm FWHM} \approx 700$ km s^{-1} forbidden line emission, $\log_{10}([\rm O\,III]/H\beta) \approx 1.1$, and high-excitation potential emission lines, such as [Fe VII] λ6086 and He II λ4686. The host galaxy exhibits a disturbed morphology with large kpc-scale tidal features, potential outflows from both nuclei, and a likely superbubble. A circular relativistic disc model cannot reproduce the asymmetric broad emission-line profiles in the brighter nucleus, but two non-axisymmetric disc models provide good fits to the broad emission-line profiles: an elliptical disc model and a circular disc + spiral arm model. Implications for the periodic nuclear transient ASASSN-14ko are discussed.

Key words: ISM: bubbles – galaxies: active – galaxies: individual: ESO 253−G003 – galaxies: kinematics and dynamics – galaxies: nuclei.

1 INTRODUCTION

Galaxy mergers are a natural consequence of Λ cold dark matter cosmology (see Somerville & Davé 2015 and references therein). Most or all galaxies host supermassive black holes (SMBHs) at their centres (e.g. Kormendy & Ho 2013) leading to SMBH interactions and mergers through cosmic time (e.g. Begelman, Blandford & Rees 1980). Merging galaxies present an ideal location for finding multiple SMBH systems (e.g. Menou, Haiman & Narayanan 2001; Cuadra et al. 2009; Khan et al. 2012) and for understanding both their evolution and their effect on the surrounding stellar environment (e.g. Kormendy & Ho 2013). Galactic mergers stir gas and dust (e.g. Springel 2000), increasing the likelihood of 'feeding' SMBHs with gas and increasing the prevalence of active galactic nuclei (AGNs) in these systems (e.g. Hopkins et al. 2006; Treister et al. 2012; Goulding et al. 2018).

AGN are thought to play an important role in galaxy evolution (see Kormendy & Ho 2013, for a review). The hard radiation spectrum photoionizes the surrounding gas, producing distinctive emission-line ratios (e.g. Veilleux & Osterbrock 1987) and regulating accretion on to the SMBH (e.g. Ciotti & Ostriker 2007; Park & Ricotti 2012). The accretion also drives outflows and/or jets into the host galaxy (e.g. Silk & Rees 1998; Ciotti & Ostriker 2001; Harrison et al. 2014; Nardini & Zubovas 2018), which interact with the galactic interstellar medium (ISM) and regulate star formation (SF; e.g. Hopkins et al. 2006; Dubois et al. 2012; Zubovas et al. 2013).

★ E-mail: tuckerma95@gmail.com
† DOE CSGF Fellow.
‡ NASA Fellow.
§ NHFP Einstein Fellow.

Merging galaxies provide a unique avenue for understanding AGN formation, especially the formation of multiple AGN systems (e.g. Fu et al. 2011; Comerford et al. 2015; Gabányi et al. 2016; Benítez et al. 2019; Liu et al. 2019; Kollatschny et al. 2020). Systematic searches find higher AGN occurrence rates in merging systems than in the general field population (e.g. Surace et al. 1998; Schmitt 2001; Ellison et al. 2011; Gao et al. 2020; Secrest et al. 2020), although the results can depend on the AGN selection process (e.g. Ellison, Patton & Hickox 2015).

Interestingly, merging galaxies may also provide a new location for enhanced production rates of tidal disruption events (TDEs). Binary SMBHs are thought to increase the galactic TDE rate by up to an order of magnitude, usually through three-body interactions (e.g. Ivanov, Polnarev & Saha 2005; Chen et al. 2009; Wegg & Nate Bode 2011; Liu & Chen 2013; Li et al. 2019). Several TDE candidates have been discovered in merging systems (e.g. Tadhunter et al. 2017; Mattila et al. 2018; Kool et al. 2020), although dust obscuration complicates occurrence rate analyses. A similar enhancement of TDE production has been observed in post-starburst or 'E+A' galaxies (e.g. Arcavi et al. 2014; French, Arcavi & Zabludoff 2016; Prieto et al. 2016; French et al. 2020) which also exhibit signs of galactic mergers (e.g. Zabludoff et al. 1996; Pawlik et al. 2018; Chen et al. 2019). The increase in AGN and TDE rates is consistent with galactic mergers augmenting nuclear densities and modifying stellar dynamics in these systems, refilling the SMBH loss cone(s) (e.g. Merritt & Milosavljević 2005; Khan, Just & Merritt 2011; Kelley, Blecha & Hernquist 2017) and boosting the chances of stellar and gaseous interactions with the SMBH(s) (e.g. Mihos & Hernquist 1996; Van Wassenhove et al. 2014; Capelo et al. 2017).

Here we explore ESO 253−G003 with Multi-Unit Spectroscopic Explorer (MUSE; Bacon et al. 2010) integral-field unit (IFU) spectroscopy. ESO 253−G003 exhibits many features of a late-stage merger including two nuclei and kpc-scale tidal arms. The brighter nucleus hosts a known AGN (Véron-Cetty & Véron 2010) at $z = 0.042\,49 \pm 0.000\,08$ (Aguero, Paolantonio & Suarez 1996) and the fainter secondary nucleus has been observed in infrared (IR) imaging (Videla et al. 2013) ≈1″.7 (∼ 1.4 kpc) away from the brighter nucleus (Asmus et al. 2014).

Recently, Payne et al. (2020) reported that ASASSN-14ko, a nuclear transient in ESO 253−G003 discovered by the All-Sky Automated Survey for SuperNovae (ASASSN; Shappee et al. 2014; Kochanek et al. 2017), exhibits periodic outbursts with a negative period derivative. Payne et al. (2020) considered three scenarios to explain the recurrent flares and negative period derivative: an SMBH binary, a bound star interacting with the SMBH disc, and a partial TDE, which we summarize briefly here. An SMBH binary was disfavoured because the predicted period derivative from gravitational wave emission is an order of magnitude smaller than the observed period derivative. The bound star scenario struggles to reproduce the stability of the flare amplitudes, shapes, and durations without fine-tuning the stellar orbit and inclination of the accretion disc to our line of sight. A repeating partial TDE can, for a period of time, produce periodic self-similar flares with a period derivative consistent with the observed value without introducing new discrepancies. Thus, Payne et al. (2020) favoured the repeating partial TDE interpretation.

Using the MUSE data, we find that (1) the broad emission lines in the brighter nucleus cannot be explained with a circular disc model, and (2) the fainter nucleus also hosts an AGN. After outlining our data acquisition, reduction, and analysis methods in Section 2, this paper takes a 'small to large' approach. We first analyse spectra of the nuclei in Section 3, placing the nuclei on emission-line diagnostic diagrams and modelling the asymmetric broad emission-line profiles. Next, we analyse various galaxy-wide properties in Section 4, including the gas kinematics and emission-line ratios. In Section 5, we discuss models of the broad-line emission in the brighter nucleus to constrain the properties of ASASSN-14ko. Finally, in Section 6, we summarize our findings. Throughout our analysis we use the standard cosmological parameters of $H_0 = 70$ km s^{-1} Mpc^{-1} and $\Omega_m = 0.3$ resulting in a luminosity distance of ≈ 188 Mpc and a projected scale of ≈ 0.85 kpc arcsec^{-1}.

Table 1. *Gaia* photometry and synthetic photometry from the MUSE datacube for the photometric calibration star to the north-east of ESO 253−G003. *Gaia* filter magnitudes (*G*, *Bp*, *Rp*) are converted to conventional filters covered by the MUSE wavelength range (*V*, *r*, *R*, *i*) using the derived photometric relations (Evans et al. 2018; Riello et al. 2018). All photometry has been corrected for line-of-sight reddening $E(B-V) = 0.04$ (Schlafly & Finkbeiner 2011). Columns: (1) Filter name, (2) Effective wavelength of the filter, (3) *Gaia* filter magnitude, (4) MUSE synthetic filter magnitude, and (5) Multiplicative scale factor (see Section 2.3).

Filter	$\lambda_{\rm eff}$ [Å]	*Gaia* [mag]	MUSE [mag]	Scale
G	5836	19.07 ± 0.01		
Bp	5021	19.56 ± 0.08		
Rp	7589	18.03 ± 0.03		
V	5446	19.41 ± 0.05	20.07 ± 0.01	1.84
r	6203	19.07 ± 0.07	19.54 ± 0.01	1.54
R	6696	18.81 ± 0.05	19.22 ± 0.01	1.46
i	7673	18.63 ± 0.10	18.89 ± 0.01	1.27

2 DATA AND METHODS

2.1 MUSE observations

Our MUSE observations of ESO 253−G003 were obtained on 2015 December 02 as part of the All-weather MUse Supernova Integral-field of Nearby Galaxies (AMUSING; Galbany et al. 2016; López-Cobá et al. 2020) survey. Galbany et al. (2016) describe the observing strategy and data reduction. The MUSE observations were conducted ≈45 d after the previous ASASSN-14ko outburst (phase ∼0.4 for a period of 114 d) when the nucleus was at the quiescent optical flux level (Payne et al. 2020).

The MUSE field of view covers 1 × 1 arcmin (≈ 51 × 51 kpc at the distance of ESO 253−G003) with a spatial sampling of 0″.2 × 0″.2 (≈ 0.17 × 0.17 kpc) per spaxel. Using the bright star to the north-east of ESO 253−G003, we measure a spatial full width at half-maximum (FWHM) of 0″.8 (4 spaxels = 0.68 kpc) for the point spread function. The spectra cover 4750–9300 Å (rest wavelength ≈ 4560–8920 Å) with a spectral sampling of 1.25 Å and a resolution of R = 1750/3750 at the blue/red end of the spectrum.

2.2 Telluric corrections

The oxygen '*B* band' telluric feature at ∼ 6880 Å falls atop the [N II] λ6583 emission line at the redshift of ESO 253−G003. To prevent biased measurements of the [N II] λ6583 emission-line parameters, we apply small corrections to the O_2 absorption regions. The atmospheric molecular absorption spectrum is retrieved from the ESO Sky Model Calculator[1] for Paranal using the parameters for the time of the MUSE observations such as airmass and seasonal value

[1] https://www.eso.org/observing/etc/bin/gen/form?INS.MODE=swspectr+INS.NAME=SKYCALC

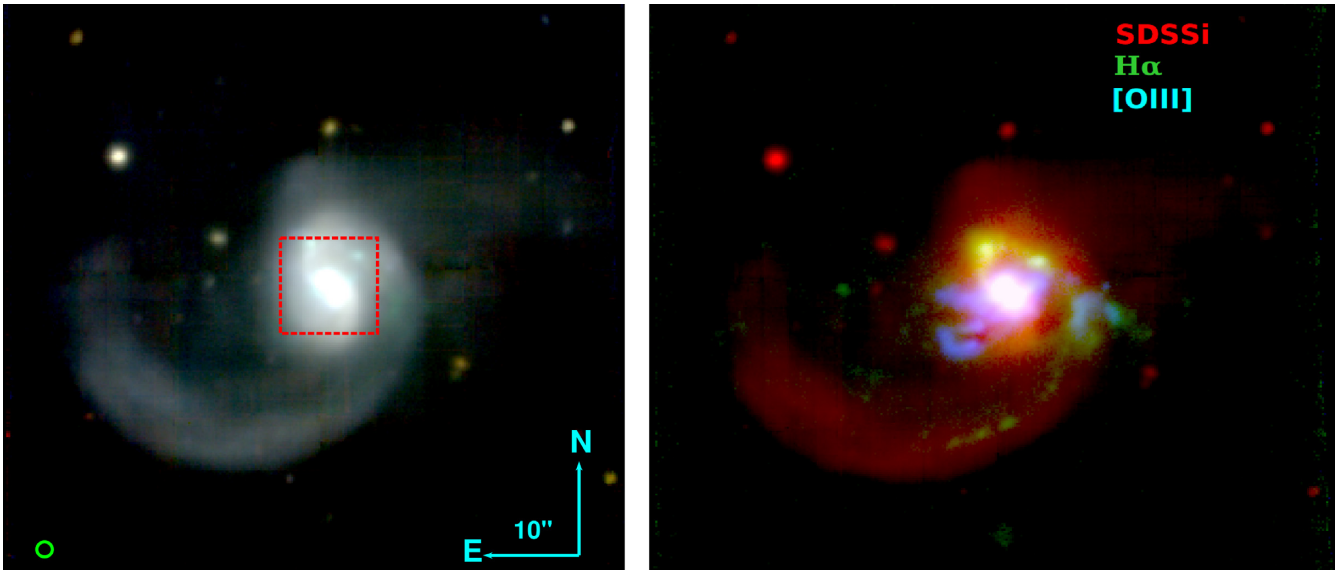

Figure 1. Broad-band (left; blue = 4800–5500 Å, green = 6600–7300 Å, red = 8400–9100 Å) and emission-line (right, blue = [O III] λ5007, green = Hα, red = SDSS *i*-band) images constructed from the MUSE datacube. The 10 arcsec image scale corresponds to a projected scale of ≈ 8.5 kpc at the distance of the galaxy. The green circle in the lower left corner represents the 0.″8 image FWHM measured using the bright star to the north-east of the galaxy. The dashed red square in the left-hand panel marks the inset shown in Fig. 2.

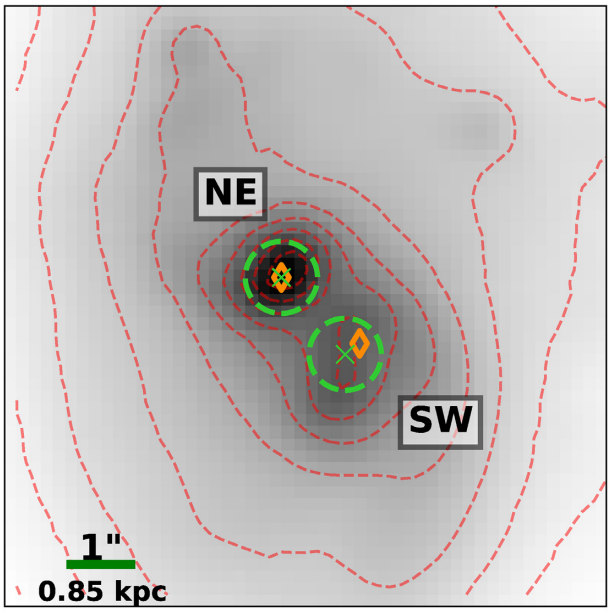

Figure 2. Zoom-in of the nuclear region of ESO 253−G003 (the red box in the left-hand panel of Fig. 1) constructed using a spectral region free from strong emission lines (λ = 5100–6100 Å). The dotted red lines are 10 logarithmically spaced surface brightness contours. Green X's mark the centres of each nucleus computed from fitting two-dimensional Gaussian profiles and the green dashed circles represent the spectral extraction apertures used in Section 3. The orange diamonds mark the locations of the MIR point sources (Asmus et al. 2014) with a small coordinate shift applied (see Section 3).

for the precipitable water vapor. We fit the molecular absorption template to the O_2 '*A* band' (λ ≈ 7590–7700Å) to determine the scaling between the template and the observations. For each spaxel in the MUSE datacube with an O_2 *A*-band signal-to-noise (S/N) ratio of ≥3, we fit the O_2 A-band absorption feature with the template scaled by a constant value and then correct the O_2 *B*-band region with the scaled template.

The derived scale factors for each spaxel are near unity ($0.86^{+0.04}_{-0.06}$, median $\pm1\sigma$), as expected for a molecular absorption spectrum tailored for the observing location. We use the known [N II] intensity ratio (≈3; Storey & Zeippen 2000) as an independent check on our corrections. Before applying the corrections, the [N II] intensity ratio was $2.1^{+0.9}_{-0.3}$ for spaxels with ≥5σ detections for both [N II] λ6548 and [N II] λ6583. After applying our corrections, the [N II] intensity ratio rises to $2.7^{+0.2}_{-0.3}$, within ∼1σ of the expected value, albeit with non-negligible scatter. Any residual issues in the correction are a subdominant source of error as we use the scaled [N II] λ6548 flux for our later calculations in Sections 3 and 4.

2.3 Photometric calibration

A major benefit of IFU observations is reliable flux calibration without needing to account for slit losses. We use the bright star to the north-east of the galaxy to estimate the absolute flux scale. The star is in the *Gaia* DR2 catalogue (ID 4799083000694906368; Gaia Collaboration2016, 2018) and we provide the photometry in Table 1. The *Gaia* filters extend beyond the MUSE wavelength range, so we convert the *Gaia* photometry to conventional filters using known photometric relations (Evans et al. 2018; Riello et al. 2018). We extracted the stellar spectrum and computed synthetic magnitudes for Johnson *V*, Johnson *R*, SDSS *r*, and SDSS *i* using filter transmission curves retrieved from the SVO filter profile service (Rodrigo, Solano & Bayo 2012).

Comparing the *Gaia* and MUSE magnitudes, we notice a wavelength-dependent offset between the predicted and observed magnitudes. We use the magnitude differences to compute a multiplicative scale factor for each filter and use a linear fit to the effective wavelengths and scale factors to place the MUSE datacube on an absolute flux scale. We conservatively estimate a ∼ 10 per cent uncertainty in the absolute flux scale based on the uncertainties in the calculated magnitude differences.

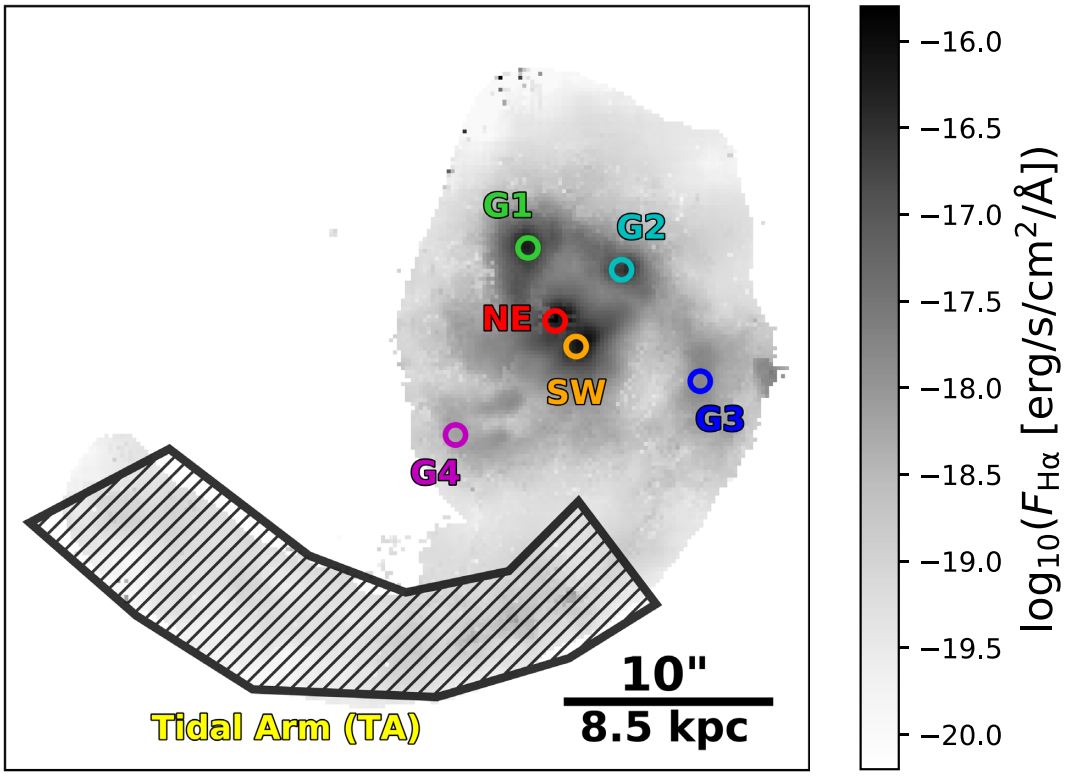

Figure 3. Spatial locations of the extracted spectra used in Sections 3 and 4 superimposed on a map of the Hα line flux.

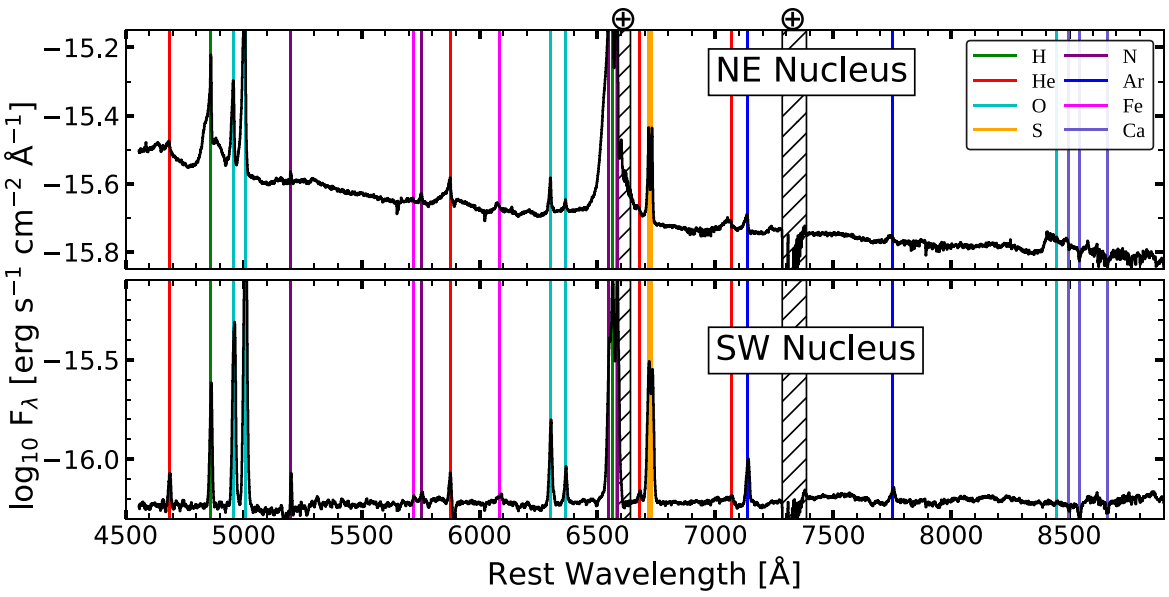

Figure 4. Spectra of the NE (top) and SW (bottom) nuclei. Major emission and absorption features are marked by coloured vertical lines. Hatched regions mark the O_2 telluric bands.

2.4 Line fitting procedure

We initially attempted to fit stellar population synthesis (SPS) models to the observed spectra (e.g. STARLIGHT; Fernandes, Leão & Lacerda 2003). However, strong emission lines contaminate the Hα and Hβ regions and the MUSE wavelength range does not cover the higher order Balmer lines (e.g. Hγ, Hδ), which are usually a better tracer of recent SF (e.g. Dressler et al. 1999). Additionally, the continuum emission is too weak to place useful constraints on the stellar absorption features. For these reasons, we choose not to fit SPS models to the observed spectra with the caveat that this introduces a low-level systematic uncertainty to all line flux measurements. We include an additional 10 per cent uncertainty in quadrature when

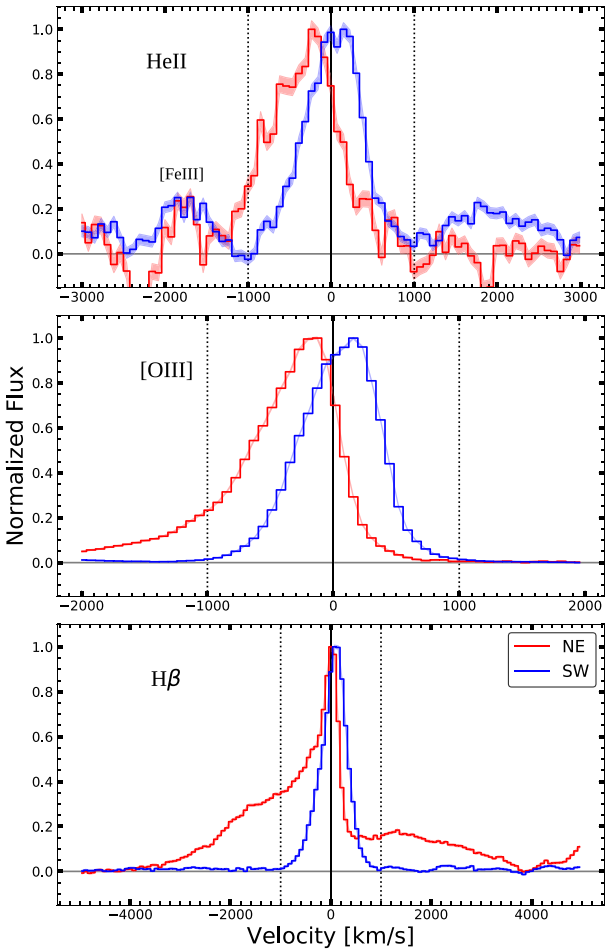

Figure 5. A velocity–space comparison of the emission-line profiles for the NE (red) and SW (blue) nuclei, including He II λ4686 (top), [O III] λ5007 (middle), and Hβ (bottom). The vertical dotted black lines in each panel span $\pm$1000 km s^{-1} and serve as a common reference between panels.

measuring emission-line fluxes. Instead of SPS models, we use low-order polynomials to estimate the spectral continuum, minimizing the normalized median absolute deviation to prevent strong emission lines from affecting the derived continuum level.

To measure the emission-line properties we fit emission-line templates to the continuum-subtracted 1D spectra. Each template has a single velocity shift v_r (relative to the systemic velocity), a velocity width $v_{\rm FWHM}$, and includes Gaussian profiles for the following emission lines typical for AGN and active galaxies: Hα, Hβ, [O III] λλ4959, 5007, [O I] λλ6300, 6363, [N II] λλ6548, 6583, and [S II] λλ6716, 6731. The flux amplitudes and velocity parameters are fit simultaneously for each spectrum and uncertainties are estimated from the covariance matrix.

The nuclear region is more complicated, as there are broad emission-line components and asymmetric line profiles. Therefore, we use multiple emission-line templates when fitting the nuclear spectra. To reduce the number of degrees of freedom in the multitemplate fitting process, we fix the [O III] λλ4959, 5007 flux ratio to 2.99 (Storey & Zeippen 2000; Dimitrijević et al. 2007) for all templates. The [N II] λλ6548, 6583 lines also have a known flux ratio of ≈3 (Storey & Zeippen 2000), but since this region is contaminated by O_2 absorption no constraint is applied. For spectra with broad-line components, we fit the isolated emission lines first ([O III], [O I], and [S II]) to measure the velocity shift and width for each template. The velocity parameters are then held fixed while fitting the Hβ and Hα + [N II] fluxes.

3 THE NUCLEI

Fig. 1 shows the broad-band (left) and emission-line (right) images for ESO 253−G003 with tidal features to the south-east and north-west of the galaxy centre. Fig. 2 provides a close-up view of the nuclear region constructed using spectral regions free from strong emission lines. We find two nuclei separated by ≈ 1.″7 = 1.4 ± 0.1 kpc, consistent with the IR imaging (Videla et al. 2013; Asmus et al. 2014), which we refer to as the 'NE' and 'SW' nuclei throughout the remainder of this paper. The NE nucleus is unresolved and roughly circular with an axial ratio of ≈1. However, the fainter SW nucleus is resolved along the major axis with an FWHM of 1.″1 ± 0.″1 but unresolved along the minor axis implying an axial ratio of $\gtrsim$1.4.

The mid-IR (MIR) locations of both nuclei (Asmus et al. 2014) are also included in Fig. 2. There is a small (≈1.″2) offset between the MUSE and MIR coordinates for the brighter NE nucleus. This is likely due to uncertainties in the absolute astrometric solution between the two images as neither the MUSE nor the MIR image are calibrated to sub-arcsec precision. Therefore, we shift the MIR coordinates so that the NE nucleus is aligned to the MUSE image in Fig. 2. This results in the MIR coordinates for the SW nucleus agreeing within 0.″3. The remaining discrepancy is attributed to the extended nature of the SW nucleus at optical wavelengths.

3.1 Spectra overview

Fig. 3 shows the spectrum extraction locations for the nuclei relative to the host galaxy along with the non-nuclear regions analysed in Section 4 with all spectra extracted with an aperture diameter equal to the spatial FWHM (0.″8). Fig. 4 shows the spectra for both NE and SW nuclei with prominent absorption and emission features labelled. The nuclei share many emission lines including strong permitted emission from H and He and forbidden emission lines from [O III], [O I], [N I], [N II], and [S II], as is typical of AGN and active galaxies (e.g. Ho, Filippenko & Sargent 1995). Notable emission lines include [Ar III], which is a reliable metallicity tracer (e.g. Arellano-Córdova et al. 2020; Kojima et al. 2020), and He II λ4686, which can be used as an AGN diagnostic line (Shirazi & Brinchmann 2012). Notable absorption lines include the Na I doublet and all three components of the Ca II near-IR (NIR) triplet.

While the nuclei share many of the same spectral features, the velocity parameters of the emission lines differ significantly. Fig. 5 compares the line profiles for Hβ, [O III] λ5007, and He II λ4686 between the two nuclei. The NE nucleus exhibits strong broad-line emission for Hα, Hβ, and He I λ5876Å. There are two broad-line emission components, each with $v_{\rm FWHM} \sim 2500$ km s^{-1} and separated by $\sim$ 3000 km s^{-1}. The SW nucleus has no evident broad-line emission component but the velocity widths for the emission lines are of order ≈700 km s^{-1}, too broad for emission from H II regions.

Of particular interest is the detection of the coronal [Fe VII] line in the SW nucleus, as shown in Fig. 6. The presence of coronal lines imply an abundance of high-energy photons as the $\gtrsim$ 100 eV ionization potentials (e.g. Penston et al. 1984) require a hard radiation spectrum typically associated with AGN (e.g. Prieto & Viegas 2000; Goulding & Alexander 2009). [Fe VII] is also observed in the NE

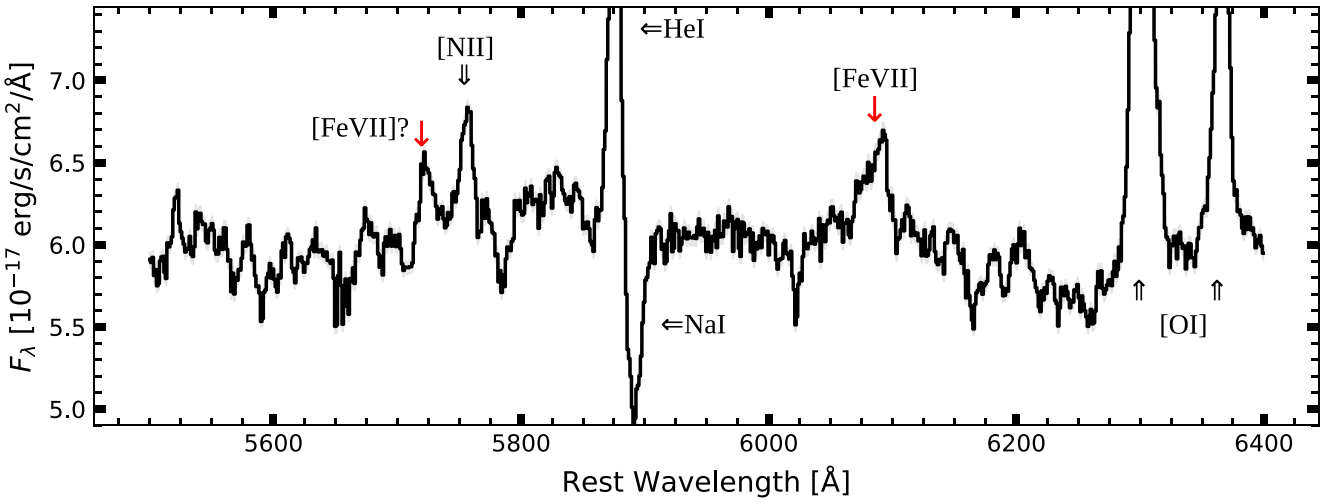

Figure 6. Portion of the spectrum for the SW nucleus from Fig. 4 covering the two prominent [Fe VII] lines. Red arrows indicate the rest wavelength locations for [Fe VII] λ5720 and [Fe VII] λ6086 emission lines and black arrows mark other spectral features typical of galaxies and AGN. The [Fe VII] λ6086 line is detected at high significance, but the [Fe VII] λ5720 line is stronger and narrower than expected (based on the [Fe VII] λ6086 line), so we consider the detection of [Fe VII] λ5720 tentative.

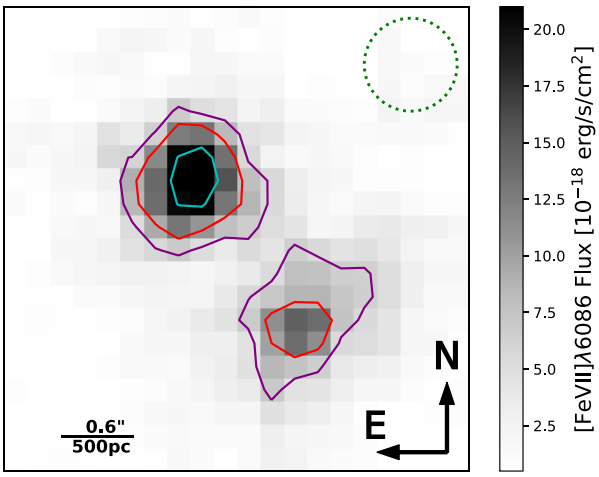

Figure 7. Spatial map of the continuum-subtracted [Fe VII] λ6086 line flux. Blue, red, and purple contours represent flux levels of $(6, 10, 20) \times 10^{-18}$ erg s^{-1} cm^{-2} and the dotted green circle signifies the spatial FWHM.

nucleus, but the presence of broad emission lines already provides robust evidence for an AGN in the brighter nucleus.

The detection of [Fe VII] provides tentative evidence for the presence of an AGN in the SW nucleus. However, the AGN in the NE nucleus also produces high-energy photons which could photoionize gas in the SW nucleus similar to ionization cones seen in other systems (e.g. Wilson et al. 1993). To test this hypothesis, Fig. 7 shows the spatial distribution of the continuum-subtracted [Fe VII] λ6086 line flux. If the [Fe VII] λ6086 emission in the SW nucleus is produced by photons originating from the NE nucleus, we would expect the [Fe VII] emission to be extended along the axis connecting the nuclei. Instead, we find similar results to the continuum image in Fig. 2: the NE nucleus is a point-source, whereas the SW nucleus is slightly extended to the north-west and consistent with a point-source at $\approx 2\sigma$.

It is possible that the gas densities are too low to produce [Fe VII] λ6086 between the nuclei in Fig. 7. However, coronal lines are typically detected within ~ 200 pc of the AGN (e.g. Prieto, Marco & Gallimore 2005; Müller-Sánchez et al. 2011; Gravity Collaboration 2021), whereas the NE and SW nuclei are separated by ≈ 1.4 kpc. Additionally, the observed $v_{\rm FWHM} \approx 400$ km s^{-1} for [Fe VII] λ6086 is consistent with coronal-line velocities observed in individual AGN (e.g. Rodríguez-Ardila et al. 2011; Cerqueira-Campos et al. 2021). Therefore, we find compelling evidence that the SW nucleus hosts an AGN. Future adaptive-optics assisted IFU spectroscopy, especially in the NIR, will place direct constraints on the spatial extent of the coronal-line emission for both nuclei (e.g. Mazzalay et al. 2013).

3.2 Emission-line diagnostics

As discussed in Section 2.4, we fit the spectra of the NE and SW nuclei with multiple emission-line templates. Fig. 8 shows that the SW spectrum is well fitted by two emission templates. A single emission template fails to adequately fit the complex line profiles (e.g. Hβ, [O I]), whereas using three templates only leads to marginal improvement. The NE spectrum, shown in Fig. 9, is more complicated. Utilizing only one or two emission templates fails to fit the [O III] profiles and other forbidden emission lines simultaneously, as the asymmetric blue wing of the [O III] profile (see Fig. 5) 'pulls' the templates away from the line centre for [S II], [O I], and Hβ. We find that three emission templates are needed to adequately fit the forbidden emission lines, although the broadest template (NE-3, $v_r \approx -650$ km s^{-1}, $v_{\rm FWHM} \approx 1300$ km s^{-1}) contributes almost zero flux for the [O I] and [S II] emission lines. In addition to the three templates, the NE Hβ line exhibits a complex double-peaked broad emission profile (Fig. 5, bottom panel). The blue- and red-shifted broad-line components are each approximated with a Gaussian profile, denoted 'broad1' and 'broad2' in Fig. 9.

After fitting each of the emission components for the NE and SW nuclei, we attempt to discern the ionizing source for each nucleus by placing the emission-line ratios on the classical BPT diagrams (Baldwin, Phillips & Terlevich 1981; Veilleux & Osterbrock 1987; Kewley et al. 2001; Kauffmann et al. 2003). The BPT classification scheme includes SF (sometimes denoted as H II), AGN, composite (a

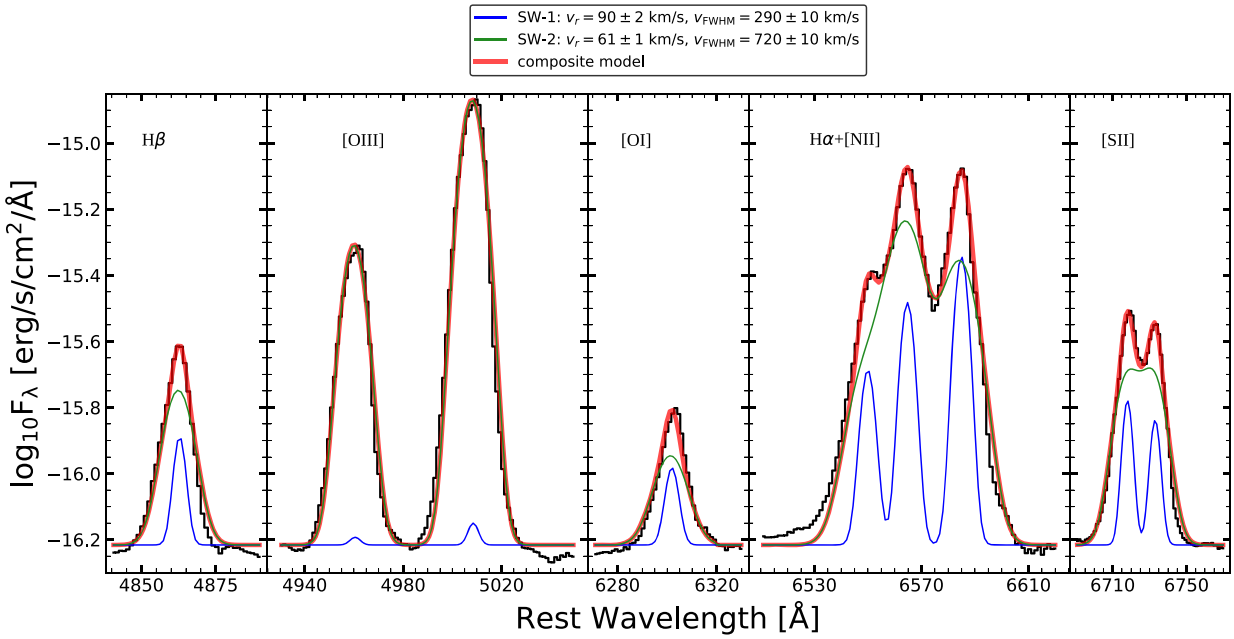

Figure 8. Emission-line decomposition for the SW nucleus. All emission lines are fitted simultaneously with the [O III] line ratio fixed (see Section 2.4).

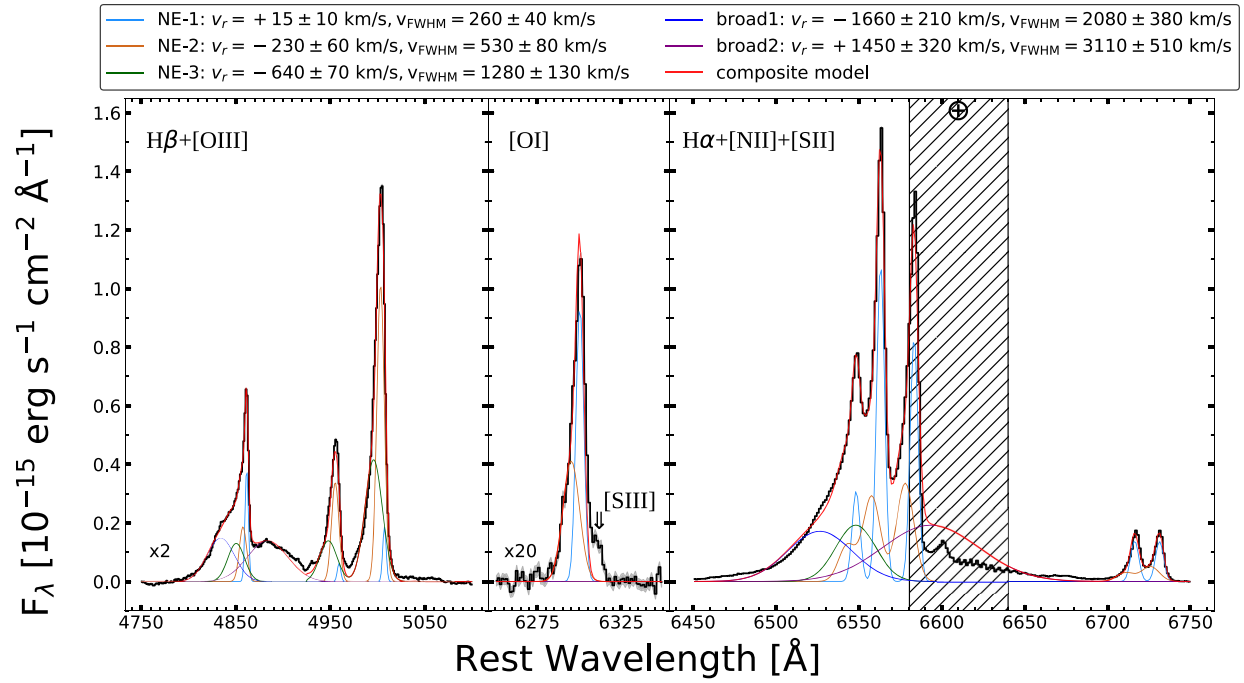

Figure 9. Emission-line decomposition for the NE nucleus. The left-hand and middle panels are scaled by a multiplicative factor given in the lower left for visual clarity. The hatched region marks wavelength regimes contaminated by telluric absorption and are excluded from the fitting process.

combination of SF and AGN ionization), and Low Ionization Narrow Emission-line Regions (LINERs). The ionization mechanism for LINERs is still debated, with proposed ionization sources including shocks from merger-induced tidal forces (e.g. Monreal-Ibero et al. 2010; Rich, Kewley & Dopita 2011), dusty or obscured AGN (e.g. Groves, Dopita & Sutherland 2004; González-Martín et al. 2009), old stellar populations (Sarzi et al. 2005), starburst-driven shocks (e.g. Olsson et al. 2007), AGN-driven shocks (e.g. Cheung et al. 2016; Molina et al. 2018), or some combination of these processes (Kewley et al. 2006; Davies et al. 2014; D'Agostino et al. 2019). We choose not to analyse each template separately as this implicitly assumes the underlying gas velocity distribution. Instead, we sum the flux from all the templates for each line measurement.

Fig. 10 shows the line ratios for both nuclei as well as line ratios for the other regions in the galaxy (Fig. 3), which are discussed in Section 4. Based on the emission-line ratios, the SW nucleus is consistent with AGN photoionization in all three BPT diagrams, whereas the NE nucleus falls along the AGN or SF boundary.

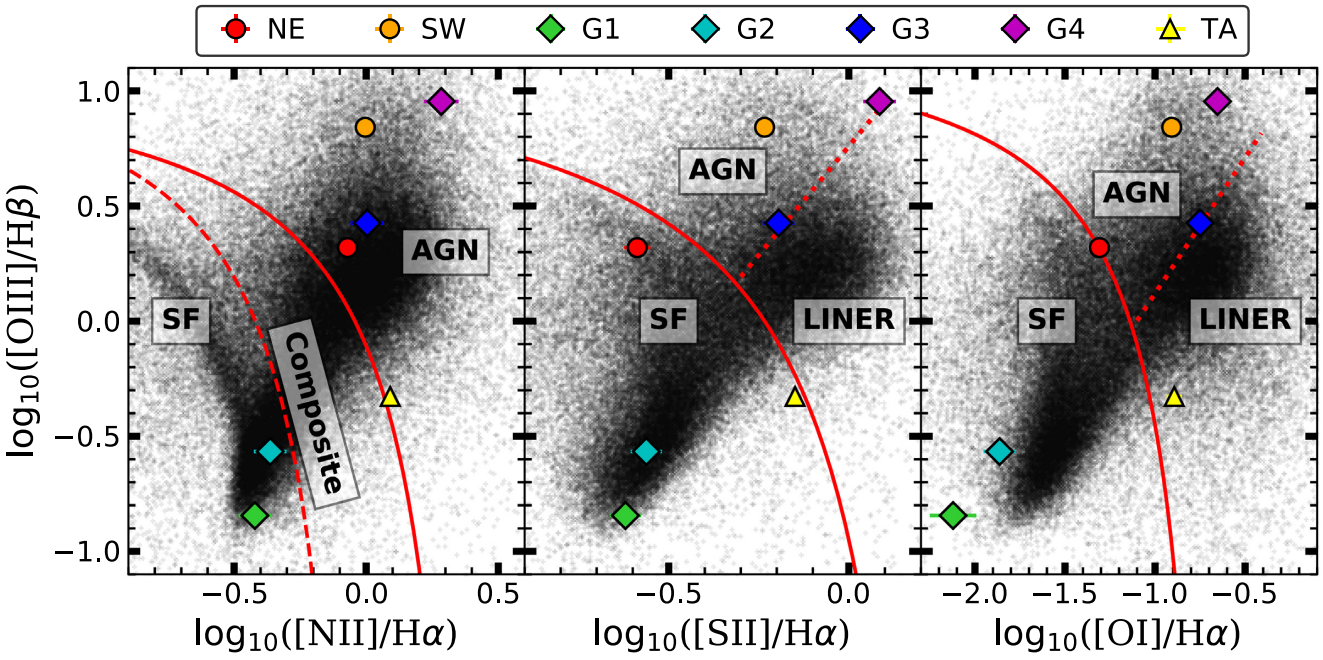

Figure 10. Emission-line diagnostic diagrams for the nuclei (circles) and selected regions within the galaxy (diamonds) compared to SDSS galaxies from the MPA-JHU catalogue (black points; York et al. 2000; Brinchmann et al. 2004). Hβ is undetected in the Tidal Arm spectrum so we place a lower limit on $\log_{10}$([O III]/Hβ) signified by the upwards triangle. The red classification lines are taken from Kewley et al. (2001) and Kauffmann et al. (2003).

In addition to the classical BPT diagrams, the nuclei also occupy parameter spaces associated with AGN in the '$W_{\rm H\alpha}$ versus [N II]/Hα' (WHAN) diagram (Cid Fernandes et al. 2011) and the He II λ4686 classification diagram (Shirazi & Brinchmann 2012).

Finally, we note that the AGN designation for both nuclei is independent of our choice to analyse the templates collectively. The NE nucleus has broad-line emission components which is robust evidence for an AGN regardless of the emission-line ratios (e.g. Stern & Laor 2013). If the SW-1 and SW-2 templates are analysed separately, the SW-2 template is consistent with AGN photoionization in the emission-line diagnostic diagrams, and exhibits line widths of $\approx$700 km s^{-1}. Conversely, the narrower ($v_{\rm FWHM} \approx 90$ km s^{-1}) SW-1 template has a mixture of SF and LINER classifications. Thus, both nuclei have spectral signatures of AGN regardless of the spectral analysis method.

3.3 Modelling the NE broad-line emission

The profiles of the broad Balmer lines from the NE nucleus appear double-peaked (Fig. 5), which is usually interpreted as emission from a relativistic accretion disc around the SMBH (e.g. Chen & Halpern 1989; Eracleous, Lewis & Flohic 2009). Although the profiles of lines from the surface of an axisymmetric disc are asymmetric because of relativistic effects, a wider variety of profile asymmetries is possible if the discs are non-axisymmetric (e.g. if the streamlines are elliptical or if spiral structure is present in a circular disc). To test if the broad-line components in the NE spectrum can be interpreted as arising from a disc, we fit disc models to the observed broad-line components. Due to the complexity of the narrow-line emission, only the broad-line emission is included in the modelling process and the models do not account for the narrow emission-line components.

We first attempted to fit a circular disc model (Chen & Halpern 1989) to the broad-line emission components in the NE spectrum. However, Fig. 11 shows that a circular disc produces a double-peaked broad-line profile with only mild asymmetries. The resulting Hβ residuals have a blue-shifted flux excess out to $v_r \sim -2500$ km s^{-1}, far higher than the blue-shifted wings of the [O III] profiles, which only extend to $v_r \sim -2000$ km s^{-1}. Instead, the asymmetry of the broad-line profile leads to a disc model that is non-axisymmetric with two configurations providing adequate results: an elliptical disc (Fig. 12) or a circular disc with a spiral arm (Fig. 13) model.

The elliptical disc model, as described in Eracleous et al. (1995), consists of nested ellipses with their major axes aligned and a fixed eccentricity e. The line-emitting portion of the disc extends between inner and outer pericenter distances $\tilde{\xi}_1$ and $\tilde{\xi}_2$ (measured in units of the gravitational radius $r_{\rm g} \equiv GM_\bullet/c^2$, where $M_\bullet$ is the mass of the SMBH). The perpendicular to the disc makes an angle i with the line of sight (the inclination angle) and the major axis of the disc makes an angle φ_0 with the projection of the line of sight in the disc plane (measured counter-clockwise, between apocenter direction and the direction of the observer, as shown in the top panel of Fig. 12). The line emissivity of the disc follows a power law with radius of the form $\epsilon \propto r^{-q}$, to describe photoionization of the surface layers by energetic photons from the vicinity of the black hole. The local profile of the emission line is taken to be a Gaussian of velocity dispersion σ to describe the effects of electron scattering and/or local turbulent motions. This model has been used to describe emission-line profiles observed in the spectra of TDEs (e.g. Holoien et al. 2019, and references therein). It may be appropriate in this case, if a transient disc is being formed out of the debris released by the tidal disruption of a star (i.e. the interpretation favoured by Payne et al. 2021). In this scenario, the line profile can vary as the structure of the accretion flow changes (see Holoien et al. 2019, and references therein).

The spiral arm model, described in Gilbert et al. (1999) and Storchi-Bergmann et al. (2003), has a 1-arm spiral emissivity pattern

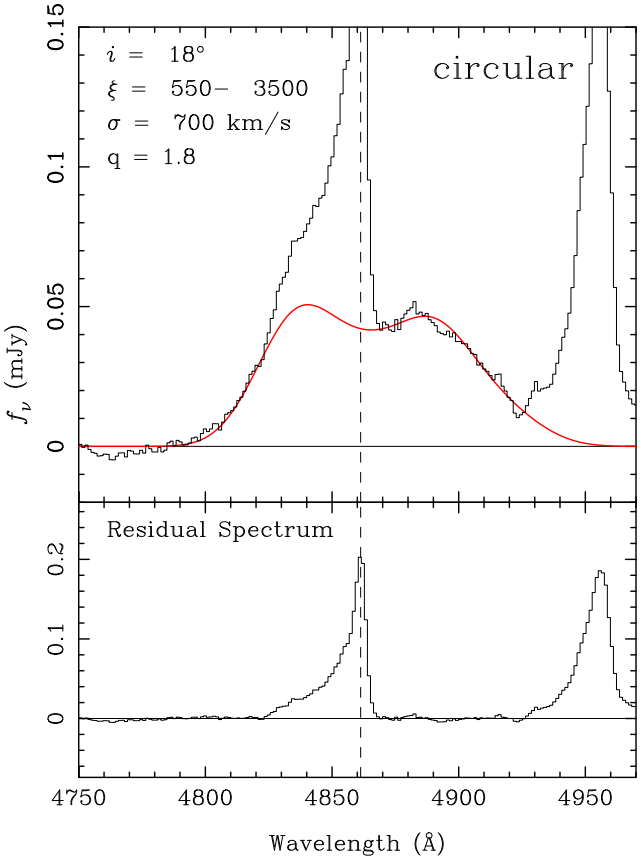

Figure 11. Best-fitting broad-line emission profile (top) and corresponding residual spectrum (bottom) for a circular relativistic disc. The narrow emission components are not included in the fitting process due to their complexity and are present in the residual spectrum (bottom panel). The circular disc model does not adequately reproduce the asymmetry of the broad-line emission profile, resulting in a blue-shifted tail in the narrow component of the Hβ line.

superimposed on the axisymmetric emissivity pattern of a circular disc. In this model, the axis of the underlying disc makes an angle i with the line of sight, the line emitting portion of the disc lies between radii ξ_1 and ξ_2 (in units of r_g), and has an axisymmetric emissivity of the form $\epsilon \propto r^{-q}$. The local line profile is a Gaussian of velocity dispersion σ. Atop the disc is a 1-arm logarithmic spiral pattern that extends between radii $\xi_{sp,1}$ and $\xi_{sp,2}$ (in units of r_g) with an angular width δ and a pitch angle p (the angle between the spiral arm and the outer rim of the disc; $p < 0$ for a trailing spiral). The azimuth of the spiral arm, extrapolated to the outer radius of the disc, is φ_0. The spiral pattern is brighter than the underlying disc by a factor A. The spiral arm model has been used to describe the variability of AGN line profiles more generally (e.g. Lewis, Eracleous & Storchi-Bergmann 2010; Schimoia et al. 2017). Spiral patterns can grow and precess on time-scales comparable to a few dynamical times (e.g. Adams, Ruden & Shu 1989; Shu et al. 1990), causing the line profile to vary accordingly.

After removing the continuum, we fit each of the models to the Hβ profile. The best fitting for each model is determined by visual inspection and we do not attempt an exhaustive search of the parameter space, as this level of detailed modelling is beyond the scope of the present work. However, we show that the disc geometry must be non-axisymmetric, if the double-peaked profiles arise from the same emission source.

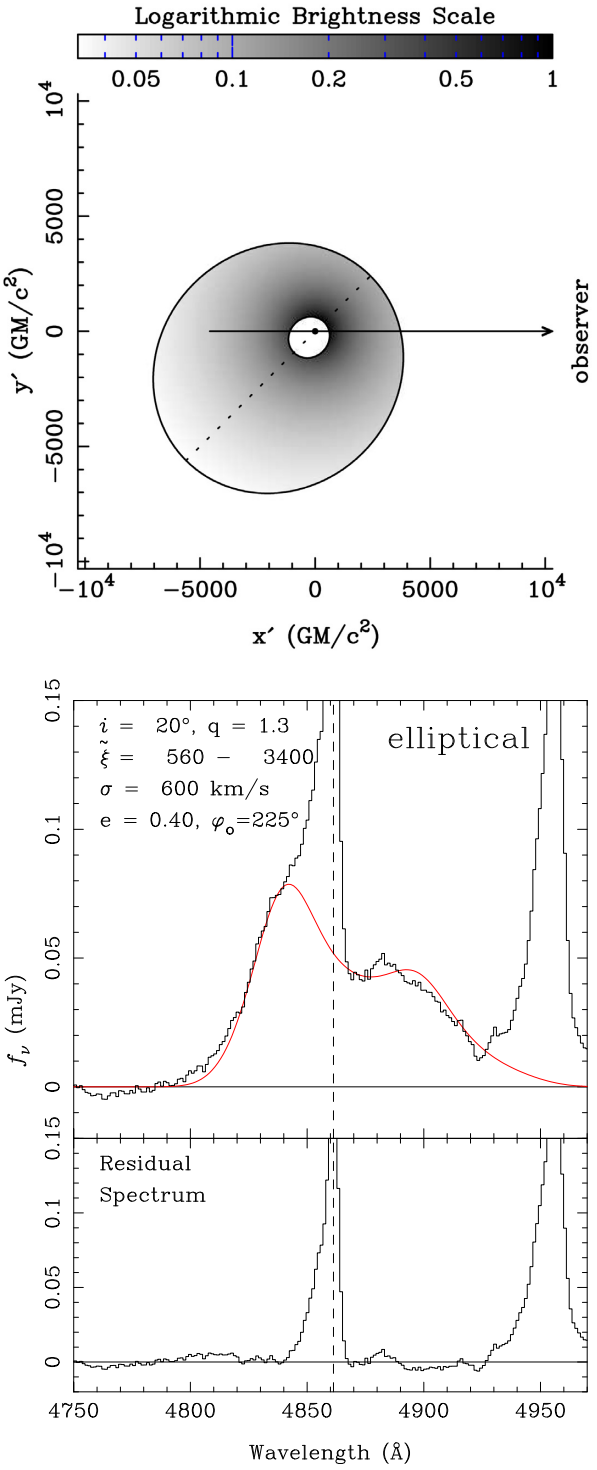

Figure 12. Elliptical-disc model for the double-peaked broad emission lines in the NE nucleus including geometric diagram (top) and the corresponding emission-line profile (bottom). The dashed line in the top panel shows the major axis of the elliptical streamlines. The parameters of the elliptical-disc model are provided in the lower panel and the notation is explained in Section 3.3 of the text.

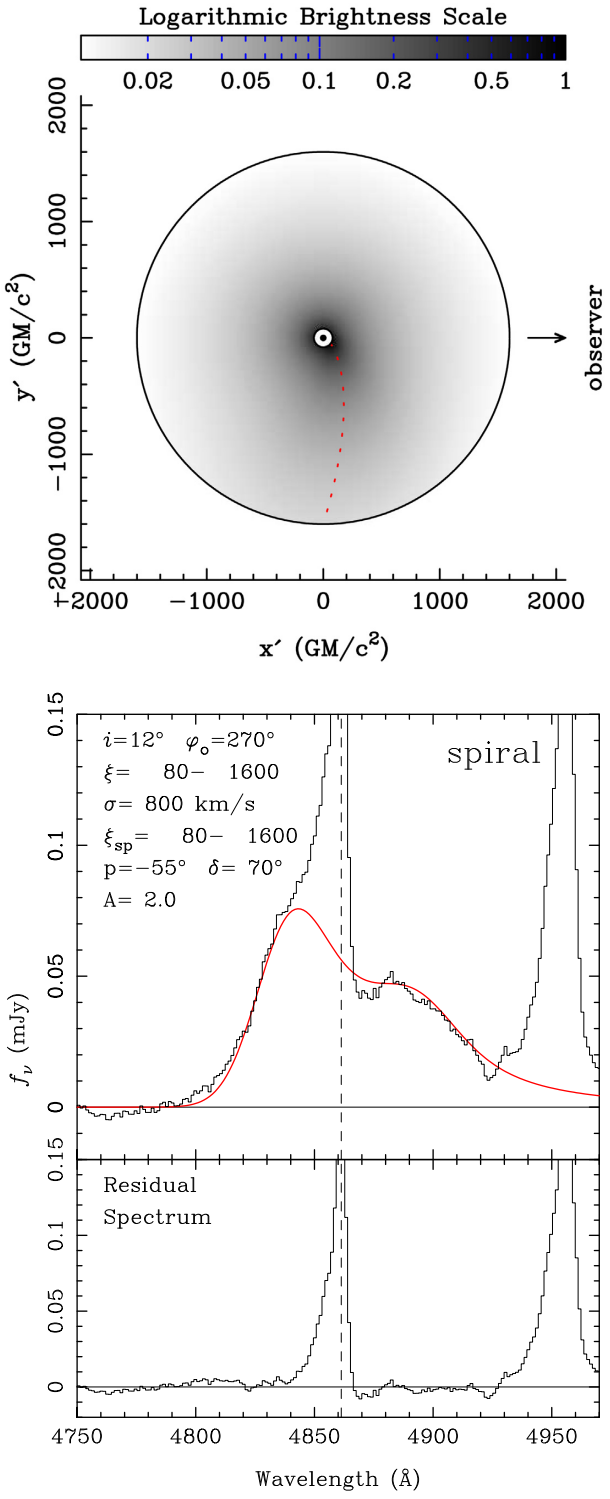

Figure 13. Spiral-arm model for the double-peaked broad-line emission profile in the NE nucleus including geometric diagram (top) and the corresponding emission-line profile (bottom). The spiral arm location is marked by a dotted red line in the top panel. The parameters for the spiral-arm model are provided in the lower panel and the notation is explained in Section 3.3 of the text.

Table 2. Velocity shift v_r and velocity width $v_{\rm FWHM}$ values for each of the non-nuclear regions marked in Fig. 3.

Location	v_r [km s^{-1}]	$v_{\rm FWHM}$ [km s^{-1}]
G1	44 ± 1	154 ± 1
G2	94 ± 1	136 ± 1
G3	40 ± 2	291 ± 4
G4	31 ± 3	247 ± 6
Tidal arm	42 ± 3	217 ± 6

4 GALAXY-WIDE PROPERTIES

Considering the unique nature of ASASSN-14ko and our discovery of a second AGN in the system, we next investigate the surrounding galactic environment. The spectral extraction locations, labelled G1-G4 and Tidal Arm for clarity, are shown in Fig. 3 and coincide with regions of strong line emission in Fig. 1. As described in Section 2.4, each 1D spectrum is fitted with a single emission-line template after fitting and subtracting a low-order polynomial continuum. The gas kinematics are derived from single-spaxel spectra, but we extract specific regions for the BPT analysis to increase the S/N ratio when measuring emission-line parameters. Table 2 provides the best-fitting v_r and $v_{\rm FWHM}$ values for each non-nuclear location.

Similar to our analysis of the nuclei, we attempt to discern the ionization source for each location by placing the spectra on the classical BPT diagrams in Fig. 10. The line ratios for the non-nuclear locations occupy various regions in the diagnostic diagrams suggesting a combination of ionizing mechanisms, as expected for a late-stage merger (e.g. Rich, Kewley & Dopita 2015).

Fig. 14 shows the derived gas kinematics. There is no clear overarching structure in the gas velocity map which would indicate coherent rotation and could be used to infer a dynamical galaxy mass. Instead, there are two potential large-scale outflows near the nuclei (OF-1 and OF-2) and a patchwork of coherent features across the galaxy. OF-1 and OF-2 overlap with the nuclei suggesting an outflow origin, but the gas velocities are only a few hundred km s^{-1} so gravitational motions cannot be excluded. Future high-resolution spectroscopy covering the Na I doublet would provide another avenue for studying outflows and bulk gas motions in this system (e.g. Heckman et al. 2000; Rupke, Veilleux & Sanders 2002; Martin 2005).

After fitting the initial velocity maps, we discovered several spaxels with above average $v_{\rm FWHM}$ in a region south or south-east of both nuclei (Fig. 14, inset). Upon closer inspection, these spaxels exhibited clear multicomponent emission features for all major emission lines, including [O III], [N II], Hα, and [S II], so we re-fit the spaxels with two emission-line templates. Fig. 15 shows the results, with the blue-shifted component tracing the large blue-shifted structure seen in Fig. 14 (OF-1), whereas the red-shifted component reveals a coherent source to the east of the nuclei. The source is marginally resolved with a spatial FWHM of $1\farcs2 \pm 0\farcs2$ although the derived spatial FWHM is consistent with a point source at $\approx 2\sigma$.

Fig. 16 shows the extracted spectrum which is well fitted by three components, two moderately narrow components (SB-1 and SB-2, $v_{\rm FWHM} \approx 350$ km s^{-1}), which are traced by the two-template fitting procedure in Fig. 15, and one broader blue-shifted component (SB-3) with $v_{\rm FWHM} \approx 750$ km s^{-1}. Of these three emission-line templates, SB-2 is the only red-shifted template and has no similar template in either of the NE or SW nuclei. Thus, we consider this a distinct emission source and consistent with a 'superbubble'. Additionally, the SB-2 template exhibits LINER characteristics in the $\log_{10}$([O I]/Hα) diagnostic diagram consistent with shock-

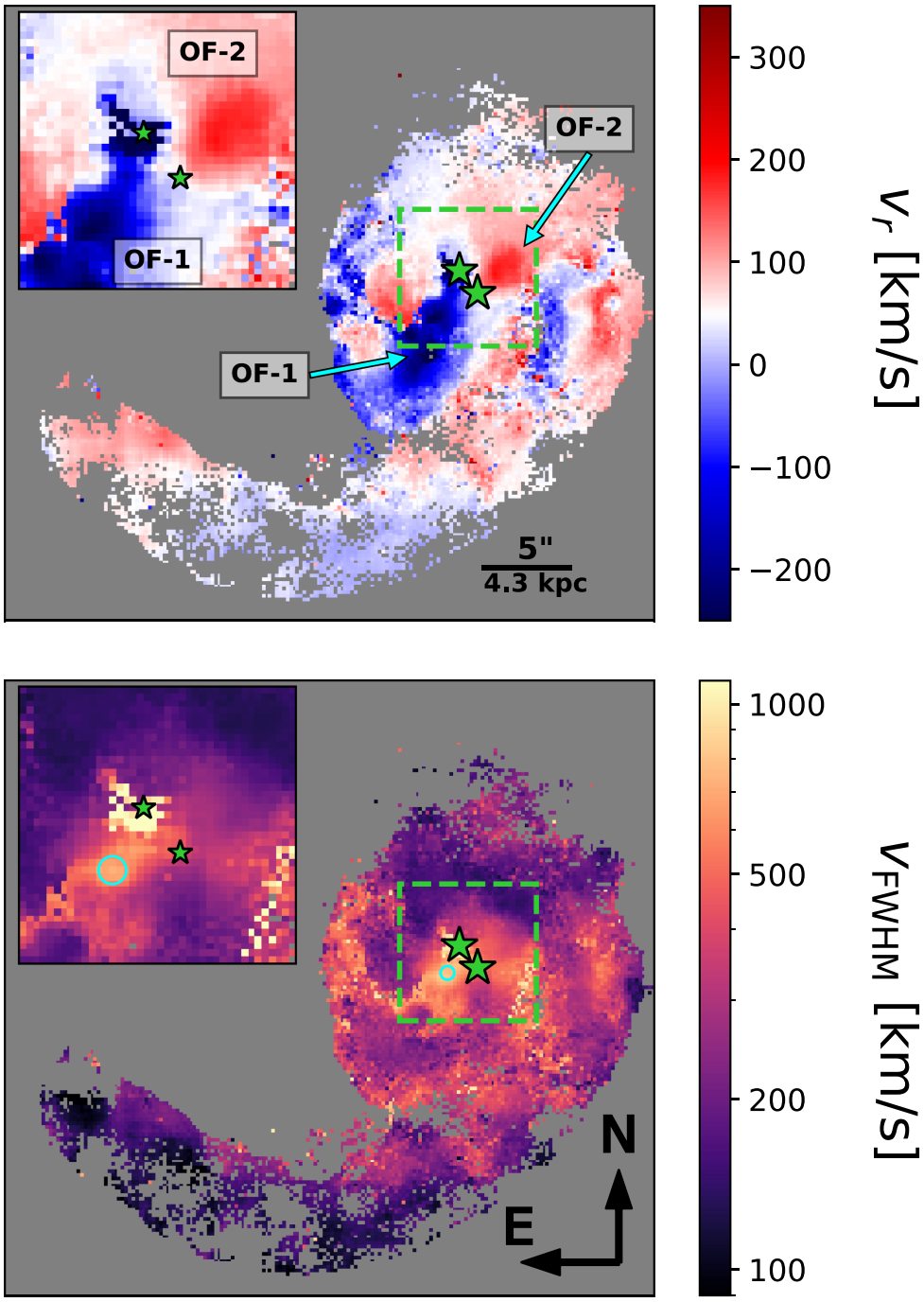

Figure 14. Maps of the mean velocity v_r (top) and line width v_{FWHM} (bottom). Note the colour map zero-point for the v_r map has been shifted by $\Delta v = -50$ km s^{-1} to highlight the velocity structure near the nuclei (green stars). The insets highlight the nuclear region inside the dashed green boxes. Two potential outflows, OF-1 and OF-2, are marked in the top panel. The blue circle in the lower panel marks the location of a potential superbubble discussed in Section 4.

excited emission (e.g. Koo & McKee 1992; Lipari et al. 2009). The $\log_{10}$([N II]/Hα) and $\log_{10}$([S II]/Hα) classification diagrams are not utilized due to the overlapping emission profiles at these locations and the subsequent uncertainty in the measured line fluxes.

5 IMPLICATIONS FOR ASASSN-14KO

Our spatial and spectral analysis of the nuclei and surrounding environment provide new insights into the intriguing nuclear transient ASASSN-14ko (Payne et al. 2021), which is located in the NE nucleus (Payne et al. 2021). Although we present strong evidence for a second AGN in the system, the SW nucleus has no influence on the evolution of ASASSN-14ko as the light traveltime between the nuclei is greater than the period of ASASSN-14ko and the sphere of influence of any SMBH is several orders of magnitude smaller than the projected separation of ≈ 1.4 kpc. In this section, we consider several hypotheses for ASASSN-14ko in the context of our new observations.

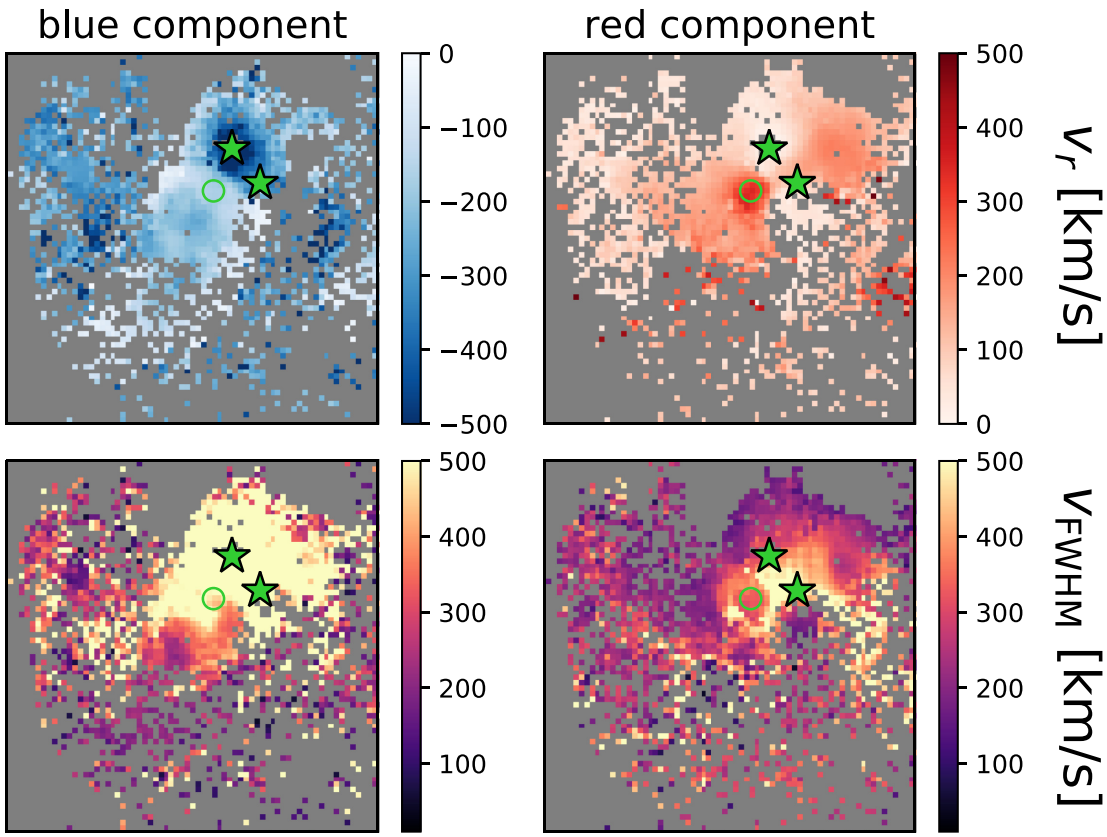

Figure 15. Two-component (left = blue-shifted, right = red-shifted) velocity maps (top: v_r, bottom: $v_{\rm FWHM}$) near the nuclei highlighting the possible detection of a superbubble. In each panel, the NE and SW nuclei are marked with green stars and the spectrum extraction radius for the potential superbubble is marked with a green circle. The superbubble appears as a resolved structure in both the v_r and $v_{\rm FWHM}$ maps for the red-shifted component (right).

Our models of the asymmetric double-peaked broad-line emission in the NE nucleus indicate that a circular relativistic disc cannot reproduce the observed emission profile (Fig. 11) and an non-axisymmetric disc is required. Two models, an elliptical disc (Fig. 12) and a spiral arm superimposed on a circular disc (Fig. 13), produce qualitatively good results. However, they differ significantly in the spatial extent of the broad-line region (BLR): $R_{\rm BLR} \approx 5000\ r_g$ for the elliptical disc compared to $R_{\rm BLR} \approx 1500\ r_g$ for the spiral arm + circular disc model.

Differentiating between these models is non-trivial, but each model will have an associated variability time-scale. The elliptical disc will precess due to relativistic effects with a period of (Eracleous et al. 1995)

$$P_{\rm precess} = 1040 \frac{1+e}{(1-e)^{3/2}} M_8 \xi_3^{5/2}\ {\rm yr}, \quad (1)$$

where e is the disc eccentricity, M_8 is the black hole mass in units of 10^8 $M_\odot$, and ξ_3 is the disc pericenter distance (ξ_1 in Section 3.3) in units of 1000 r_g. Using the parameters of the best-fitting elliptical-disc model in Fig. 12, e = 0.4 and $\xi_3 = 0.56$, and a black hole mass of $M_\bullet = 10^7 - 10^8$ $M_\odot$ derived by Payne et al. (2020), the associated precession time-scale is ≈70–700 yr.

The spiral arm model will evolve more rapidly with the variability time-scale proportional to the pattern speed of the disc. A lower limit on the variability time-scale for the spiral arm is the dynamical time-scale (Storchi-Bergmann et al. 2003; Lewis et al. 2010),

$$\tau_{\rm dyn} = 200 M_8 \xi_3^{3/2}\ {\rm d}, \quad (2)$$

where M_8 and ξ_3 are the same as in equation (1). For $M_\bullet = 10^8$ $M_\odot$ and $\xi_3 = 0.8$ (corresponding to the middle of the disc in Fig. 13), the dynamical time-scale is $\tau_{\rm dyn} \approx 140$ d, remarkably close to the period of ASASSN-14ko (≈114 d). This scenario matches the partial TDE or bound star interpretations for ASASSN-14ko as each passage of the star would disturb the disc, producing a spiral arm that propagates through the disc and creates the observed asymmetries in the broad emission-line profiles. Even using the outermost edge of the disc, the dynamical time-scale is of order ∼1 yr and still ∼2 orders of magnitude smaller than the elliptical disc precession period, providing an avenue for distinguishing between these models with future spectroscopic observations.

We searched for disparities between our MUSE spectrum and the spectra of ASASSN-14ko presented by Payne et al. (2020). The spectra show differences in the shapes and strengths of the emission-line profiles. However, we could not reliably remove contamination from the SW nucleus due to ambiguities in the observing set-ups for the archival spectra (e.g. slit width, slit position angle, and atmospheric seeing). Therefore, we reserve a spectral comparison for future work and reiterate the usefulness of IFU observations for this system.

There is the possibility that the observed broad emission-line profiles do not originate from a relativistic disc, in which case the variability time-scales discussed above do not apply. Instead, the broad emission-line profiles could stem from separate emission sources such as a binary SMBH system (e.g. Gaskell 1983; Boroson & Lauer 2009; Zheng et al. 2016), where each SMBH hosts an accretion disc and produces one of the broad-line profiles, or a

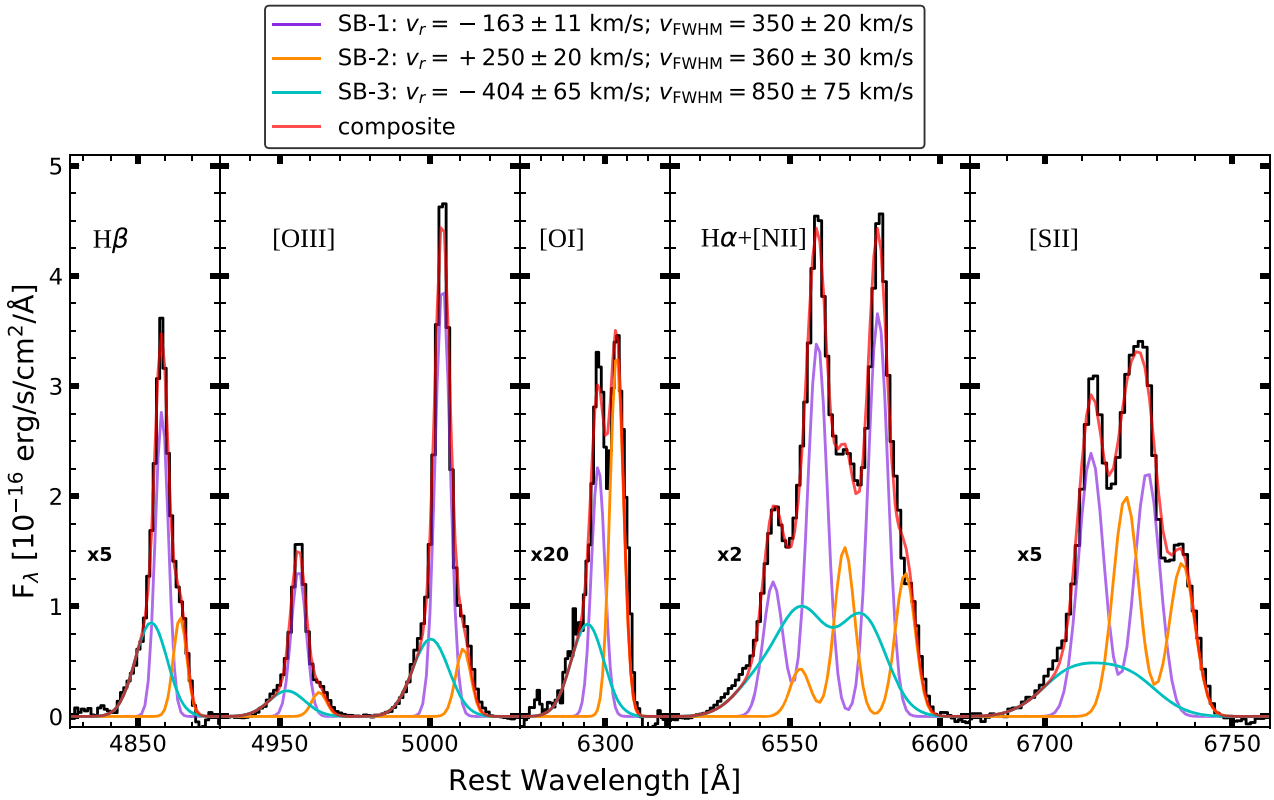

Figure 16. Extracted spectrum and emission decomposition for the potential superbubble structure labelled in Fig. 15. Some spectra are scaled by a multiplicative factor for visual clarity with scale factors noted to the left of the corresponding line profile.

biconical outflow (e.g. Zheng, Binette & Sulentic 1990; Zheng, Veilleux & Grandi 1991) where the two lobes of the outflow produce the blue- and red-shifted broad-line profiles. We find these scenarios unlikely, as both theories have repeatedly failed observational tests in other systems (see e.g. Dietrich et al. 1998; Fausnaugh et al. 2017; Runnoe et al. 2017; Doan et al. 2020), but our current data cannot eliminate them from consideration.

6 CONCLUSION

We analyse MUSE data of ESO 253−G003 which exhibits many signatures of a late-stage merger, including a prominent tidal arm and two nuclei. This galaxy also hosts the periodic nuclear transient ASASSN-14ko (Payne et al. 2020), motivating a better understanding of its environment. By combining galaxy-wide properties with an in-depth analysis of the nuclei emission characteristics, we provide several important insights into the environment and characteristics of the merger.

The spectra of the two nuclei have notable differences in their velocity profiles (Fig. 5). The NE nucleus, which hosts the periodic nuclear transient ASASSN-14ko (Payne et al. 2021), exhibits asymmetric double-peaked broad emission lines for Hβ, which we model with both axisymmetric and non-axisymmetric relativistic disc models. The broad-line profile cannot be reproduced with a circular disc (Fig. 11), but two non-axisymmetric disc models provide good fits to the broad-line profile: an elliptical disc (Fig. 12) or a circular disc with a spiral arm (Fig. 13). It seems inevitable that the interoutburst line profiles must evolve due to orbital precession, if nothing else (see Section 5). High-quality phase-resolved spectroscopy over many cycles is required to advance our understanding beyond these initial observations and speculations. However, due to the complex host-galaxy morphology and the presence of dual AGN, care should be taken when planning future observations. The efficacy of slit spectroscopy will depend heavily on the width and orientation of the slit, and we suggest IFU observations when possible to alleviate these difficulties.

The fainter SW nucleus also clearly hosts an AGN. The emission-line ratios for the SW nucleus are consistent with AGN photoionization in diagnostic diagrams (Fig. 10) and the $v_{FWHM} \approx 700$ km s^{-1} emission profiles are too broad for SF and too luminous for shocks. There is a potential red-shifted outflow originating from the SW nucleus (OF-2 in Fig. 14), suggestive of an accretion source. Finally, the detection of high-ionization lines such as coronal [Fe VII] λ6086 (Fig. 6) and broad He II λ4686 (Fig. 5) require the ultraviolet and X-ray continuum emission of an AGN.

The surrounding galactic environment also exhibits several features of an AGN merger. Velocity maps (Fig. 14) reveal likely outflows from the nuclear region extending for several kpc into the surrounding ISM and a potential AGN-driven superbubble. The host galaxy exhibits many locations with AGN and LINER emission-line ratios, consistent with an AGN merger producing large-scale outflow signatures and shocks. Future high-resolution optical spectroscopy centred on the Na I doublet and/or radio observations will provide further constraints on outflows, especially for cold gas not probed by our emission-line analyses.

ACKNOWLEDGEMENTS

We thank the referee for constructive comments and M. Togami for useful discussions.

MAT acknowledges support from the DOE CSGF through grant no. DE-SC0019323. BJS and CSK are supported by NSF grant no. AST-1907570. BJS is also supported by NASA grant no. 80NSSC19K1717 and NSF grants AST-1920392 and AST-1911074. CSK is supported by NSF grant no. AST-181440. KAA is supported by the Danish National Research Foundation (DNRF132). Support for JLP is provided in part by FONDECYT through grant n.1191038 and by the Ministry for the Economy, Development, and Tourism's Millennium Science Initiative through grant no. IC120009, awarded to The Millennium Institute of Astrophysics, MAS. LG acknowledges financial support from the Spanish Ministry of Science, Innovation and Universities (MICIU) under the 2019 Ramón y Cajal program RYC2019-027683 and from the Spanish MICIU project PID2020-115253GA-I00. Parts of this research were supported by the Australian Research Council Centre of Excellence for All Sky Astrophysics in 3 Dimensions (ASTRO 3D), through project number CE170100013. LG was funded by the European Union's Horizon 2020 research and innovation programme under the Marie Skłodowska-Curie grant agreement No. 839090, and partially supported by the Spanish grant no. PGC2018-095317-B-C21 within the European Funds for Regional Development (FEDER). Support for TW-SH was provided by NASA through the NASA Hubble Fellowship grant no. #*HST*-HF2-51458.001-A awarded by the Space Telescope Science Institute, which is operated by the Association of Universities for Research in Astronomy, Inc., for NASA, under contract NAS5-26555.

Based on observations collected at the European Organization for Astronomical Research in the Southern Hemisphere under ESO programme 096.D-0296(A).

Facilities: VLT-MUSE.

Software: ASTROPY (Astropy Collaboration 2018), LMFIT (Newville et al. 2020), MPDAF (Bacon et al. 2016; Piqueras et al. 2017), NUMPY (Harris et al. 2020), MATPLOTLIB (Hunter 2007).

DATA AVAILABILITY

The raw and reduced MUSE datacubes are publicly available at the ESO Science Archive Facility.[2]

REFERENCES

Adams F. C., Ruden S. P., Shu F. H., 1989, ApJ, 347, 959
Aguero E. L., Paolantonio S., Suarez F., 1996, PASP, 108, 1117
Arcavi I. et al., 2014, ApJ, 793, 38
Arellano-Córdova K. Z., Esteban C., García-Rojas J., Méndez-Delgado J. E., 2020, MNRAS, 496, 1051
Asmus D., Hönig S. F., Gandhi P., Smette A., Duschl W. J., 2014, MNRAS, 439, 1648
Astropy Collaboration, 2018, AJ, 156, 123
Bacon R. et al., 2010, Proc. SPIE Conf. Ser. Vol. 7735, Ground-based and Airborne Instrumentation for Astronomy III. SPIE, Bellingham, p. 773508
Bacon R., Piqueras L., Conseil S., Richard J., Shepherd M., 2016, MPDAF: MUSE Python Data Analysis Framework. Available at: http://ascl.net/1611.003
Baldwin J. A., Phillips M. M., Terlevich R., 1981, PASP, 93, 5
Begelman M. C., Blandford R. D., Rees M. J., 1980, Nature, 287, 307
Benítez E. et al., 2019, MNRAS, 490, 5521
Boroson T. A., Lauer T. R., 2009, Nature, 458, 53
Brinchmann J., Charlot S., White S. D. M., Tremonti C., Kauffmann G., Heckman T., Brinkmann J., 2004, MNRAS, 351, 1151
Capelo P. R., Dotti M., Volonteri M., Mayer L., Bellovary J. M., Shen S., 2017, MNRAS, 469, 4437
Cerqueira-Campos F. C., Rodríguez-Ardila A., Riffel R., Marinello M., Prieto A., Dahmer-Hahn L. G., 2021, MNRAS, 500, 2666
Chen K., Halpern J. P., 1989, ApJ, 344, 115
Chen X., Madau P., Sesana A., Liu F. K., 2009, ApJ, 697, L149
Chen Y.-M. et al., 2019, MNRAS, 489, 5709
Cheung E. et al., 2016, Nature, 533, 504
Cid Fernandes R., Stasińska G., Mateus A., Vale Asari N., 2011, MNRAS, 413, 1687
Ciotti L., Ostriker J. P., 2001, ApJ, 551, 131
Ciotti L., Ostriker J. P., 2007, ApJ, 665, 1038
Comerford J. M., Pooley D., Barrows R. S., Greene J. E., Zakamska N. L., Madejski G. M., Cooper M. C., 2015, ApJ, 806, 219
Cuadra J., Armitage P. J., Alexander R. D., Begelman M. C., 2009, MNRAS, 393, 1423
D'Agostino J. J., Kewley L. J., Groves B. A., Medling A., Dopita M. A., Thomas A. D., 2019, MNRAS, 485, L38
Davies R. L., Rich J. A., Kewley L. J., Dopita M. A., 2014, MNRAS, 439, 3835
Dietrich M. et al., 1998, ApJS, 115, 185
Dimitrijević M. S., Popović L. Č., Kovačević J., Dačić M., Ilić D., 2007, MNRAS, 374, 1181
Doan A., Eracleous M., Runnoe J. C., Liu J., Mathes G., Flohic H. M. L. G., 2020, MNRAS, 491, 1104
Dressler A., Smail I., Poggianti B. M., Butcher H., Couch W. J., Ellis R. S., Oemler, Augustus J., 1999, ApJS, 122, 51
Dubois Y., Devriendt J., Slyz A., Teyssier R., 2012, MNRAS, 420, 2662
Ellison S. L., Patton D. R., Mendel J. T., Scudder J. M., 2011, MNRAS, 418, 2043
Ellison S. L., Patton D. R., Hickox R. C., 2015, MNRAS, 451, L35
Eracleous M., Livio M., Halpern J. P., Storchi-Bergmann T., 1995, ApJ, 438, 610
Eracleous M., Lewis K. T., Flohic H. M. L. G., 2009, New Astron. Rev., 53, 133
Evans D. W. et al., 2018, A&A, 616, A4
Fausnaugh M. M. et al., 2017, ApJ, 840, 97
Fernandes R. C., Leão J. R. S., Lacerda R. R., 2003, MNRAS, 340, 29
French K. D., Arcavi I., Zabludoff A., 2016, ApJ, 818, L21
French K. D., Arcavi I., Zabludoff A. I., Stone N., Hiramatsu D., van Velzen S., McCully C., Jiang N., 2020, ApJ, 891, 93
Fu H. et al., 2011, ApJ, 740, L44
Gabányi K. É., An T., Frey S., Komossa S., Paragi Z., Hong X. Y., Shen Z. Q., 2016, ApJ, 826, 106
Gaia Collaboration, 2016, A&A, 595, A1
Gaia Collaboration, 2018, A&A, 616, A1
Galbany L. et al., 2016, MNRAS, 455, 4087
Gao F. et al., 2020, A&A, 637, A94
Gaskell C. M., 1983, in Swings J.-P., ed., Liege International Astrophysical Colloquia, Vol. 24, p. 473
Gilbert A. M., Eracleous M., Filippenko A. V., Halpern J. P., 1999, in Gaskell C. M., Brandt W. N., Dietrich M., Dultzin-Hacyan D., Eracleous M., eds, ASP Conf. Ser. Vol. 175, Structure and Kinematics of Quasar Broad Line Regions. Astron. Soc. Pac., San Francisco, p. 189
González-Martín O., Masegosa J., Márquez I., Guainazzi M., 2009, ApJ, 704, 1570
Goulding A. D., Alexander D. M., 2009, MNRAS, 398, 1165
Goulding A. D. et al., 2018, PASJ, 70, S37
Gravity Collaboration 2021, A&A, 648, A117
Groves B. A., Dopita M. A., Sutherland R. S., 2004, ApJS, 153, 9
Harris C. R. et al., 2020, 585, 357
Harrison C. M., Alexander D. M., Mullaney J. R., Swinbank A. M., 2014, MNRAS, 441, 3306
Heckman T. M., Lehnert M. D., Strickland D. K., Armus L., 2000, ApJS, 129, 493
Ho L. C., Filippenko A. V., Sargent W. L., 1995, ApJS, 98, 477
Holoien T. W. S. et al., 2019, ApJ, 880, 120

[2] http://archive.eso.org

Hopkins P. F., Hernquist L., Cox T. J., Di Matteo T., Robertson B., Springel V., 2006, ApJS, 163, 1
Hunter J. D., 2007, Comput. Sci. Eng., 9, 90
Ivanov P. B., Polnarev A. G., Saha P., 2005, MNRAS, 358, 1361
Kauffmann G. et al., 2003, MNRAS, 346, 1055
Kelley L. Z., Blecha L., Hernquist L., 2017, MNRAS, 464, 3131
Kewley L. J., Dopita M. A., Sutherland R. S., Heisler C. A., Trevena J., 2001, ApJ, 556, 121
Kewley L. J., Groves B., Kauffmann G., Heckman T., 2006, MNRAS, 372, 961
Khan F. M., Just A., Merritt D., 2011, ApJ, 732, 89
Khan F. M., Preto M., Berczik P., Berentzen I., Just A., Spurzem R., 2012, ApJ, 749, 147
Kochanek C. S. et al., 2017, PASP, 129, 104502
Kojima T. et al., 2021, 913, 22
Kollatschny W., Weilbacher P. M., Ochmann M. W., Chelouche D., Monreal-Ibero A., Bacon R., Contini T., 2020, A&A, 633, A79
Koo B.-C., McKee C. F., 1992, ApJ, 388, 93
Kool E. C. et al., 2020, MNRAS, 498, 2167
Kormendy J., Ho L. C., 2013, ARA&A, 51, 511
Lewis K. T., Eracleous M., Storchi-Bergmann T., 2010, ApJS, 187, 416
Li S., Berczik P., Chen X., Liu F. K., Spurzem R., Qiu Y., 2019, ApJ, 883, 132
Lipari S. et al., 2009, MNRAS, 392, 1295
Liu F. K., Chen X., 2013, ApJ, 767, 18
Liu X. et al., 2019, ApJ, 887, 90
López-Cobá C. et al., 2020, AJ, 159, 167
Martin C. L., 2005, ApJ, 621, 227
Mattila S. et al., 2018, Science, 361, 482
Mazzalay X., Rodríguez-Ardila A., Komossa S., McGregor P. J., 2013, MNRAS, 430, 2411
Menou K., Haiman Z., Narayanan V. K., 2001, ApJ, 558, 535
Merritt D., Milosavljević M., 2005, Living Rev. Relativ., 8, 8
Mihos J. C., Hernquist L., 1996, ApJ, 464, 641
Molina M., Eracleous M., Barth A. J., Maoz D., Runnoe J. C., Ho L. C., Shields J. C., Walsh J. L., 2018, ApJ, 864, 90
Monreal-Ibero A., Arribas S., Colina L., Rodríguez-Zaurín J., Alonso-Herrero A., García-Marín M., 2010, A&A, 517, A28
Müller-Sánchez F., Prieto M. A., Hicks E. K. S., Vives-Arias H., Davies R. I., Malkan M., Tacconi L. J., Genzel R., 2011, ApJ, 739, 69
Nardini E., Zubovas K., 2018, MNRAS, 478, 2274
Newville M. et al., 2020, lmfit/lmfit-py 1.0.1., Zenodo
Olsson E., Aalto S., Thomasson M., Beswick R., Hüttemeister S., 2007, A&A, 473, 389
Park K., Ricotti M., 2012, ApJ, 747, 9
Pawlik M. M. et al., 2018, MNRAS, 477, 1708
Payne A. V. et al., 2020, 910, 125
Payne A. V. et al., 2021, preprint (arXiv:2104.06414)
Penston M. V., Fosbury R. A. E., Boksenberg A., Ward M. J., Wilson A. S., 1984, MNRAS, 208, 347
Piqueras L., Conseil S., Shepherd M., Bacon R., Leclercq F., Richard J., 2017, preprint (arXiv:1710.03554)
Prieto M. A., Viegas S. M., 2000, ApJ, 532, 238
Prieto M. A., Marco O., Gallimore J., 2005, MNRAS, 364, L28
Prieto J. L. et al., 2016, ApJ, 830, L32
Rich J. A., Kewley L. J., Dopita M. A., 2011, ApJ, 734, 87
Rich J. A., Kewley L. J., Dopita M. A., 2015, ApJS, 221, 28
Riello M. et al., 2018, A&A, 616, A3
Rodrigo C., Solano E., Bayo A., 2012, SVO Filter Profile Service Version 1.0, IVOA Working Draft, Available at:https://ivoa.net/documents/Notes/SVOFPS/index.html
Rodríguez-Ardila A., Prieto M. A., Portilla J. G., Tejeiro J. M., 2011, ApJ, 743, 100
Runnoe J. C. et al., 2017, MNRAS, 468, 1683
Rupke D. S., Veilleux S., Sanders D. B., 2002, ApJ, 570, 588
Sarzi M., Rix H.-W., Shields J. C., Ho L. C., Barth A. J., Rudnick G., Filippenko A. V., Sargent W. L. W., 2005, ApJ, 628, 169
Schimoia J. S., Storchi-Bergmann T., Winge C., Nemmen R. S., Eracleous M., 2017, MNRAS, 472, 2170
Schlafly E. F., Finkbeiner D. P., 2011, ApJ, 737, 103
Schmitt H. R., 2001, AJ, 122, 2243
Secrest N. J., Ellison S. L., Satyapal S., Blecha L., 2020, MNRAS, 499, 2380
Shappee B. J. et al., 2014, ApJ, 788, 48
Shirazi M., Brinchmann J., 2012, MNRAS, 421, 1043
Shu F. H., Tremaine S., Adams F. C., Ruden S. P., 1990, ApJ, 358, 495
Silk J., Rees M. J., 1998, A&A, 331, L1
Somerville R. S., Davé R., 2015, ARA&A, 53, 51
Springel V., 2000, MNRAS, 312, 859
Stern J., Laor A., 2013, MNRAS, 431, 836
Storchi-Bergmann T. et al., 2003, ApJ, 598, 956
Storey P. J., Zeippen C. J., 2000, MNRAS, 312, 813
Surace J. A., Sanders D. B., Vacca W. D., Veilleux S., Mazzarella J. M., 1998, ApJ, 492, 116
Tadhunter C., Spence R., Rose M., Mullaney J., Crowther P., 2017, Nature Astron., 1, 0061
Treister E., Schawinski K., Urry C. M., Simmons B. D., 2012, ApJ, 758, L39
Van Wassenhove S., Capelo P. R., Volonteri M., Dotti M., Bellovary J. M., Mayer L., Governato F., 2014, MNRAS, 439, 474
Veilleux S., Osterbrock D. E., 1987, ApJS, 63, 295
Véron-Cetty M. P., Véron P., 2010, A&A, 518, A10
Videla L., Lira P., Andrews H., Alonso-Herrero A., Alexander D. M., Ward M., 2013, ApJS, 204, 23
Wegg C., Nate Bode J., 2011, ApJ, 738, L8
Wilson A. S., Braatz J. A., Heckman T. M., Krolik J. H., Miley G. K., 1993, ApJ, 419, L61
York D. G. et al., 2000, AJ, 120, 1579
Zabludoff A. I., Zaritsky D., Lin H., Tucker D., Hashimoto Y., Shectman S. A., Oemler A., Kirshner R. P., 1996, ApJ, 466, 104
Zheng W., Binette L., Sulentic J. W., 1990, ApJ, 365, 115
Zheng W., Veilleux S., Grandi S. A., 1991, ApJ, 381, 418
Zheng Z.-Y., Butler N. R., Shen Y., Jiang L., Wang J.-X., Chen X., Cuadra J., 2016, ApJ, 827, 56
Zubovas K., Nayakshin S., King A., Wilkinson M., 2013, MNRAS, 433, 3079

This paper has been typeset from a TEX/LATEX file prepared by the author.